Momentum for Catalysis: How Surface Reactions Shape the RuO2 Flat Surface State

Published Version:
Jovic Vedran, C.A. (2021). Momentum for Catalysis: How Surface Reactions Shape the RuO2 Flat Surface State. ACS CATALYSIS, 11(3), 1749-1757 [10.1021/acscatal.0c04871].

Availability:
This version is available at: https://hdl.handle.net/11585/892832 since: 2022-08-20

Published:

DOI: http://doi.org/10.1021/acscatal.0c04871

Vedran Jovic, Armando Consiglio, Kevin E. Smith, Chris Jozwiak, Aaron Bostwick, Eli Rotenberg, Domenico Di Sante, and Simon Moser, *Momentum for Catalysis: How Surface Reactions Shape the RuO2 Flat Surface State*, ACS Catalysis 2021 11 (3), 1749-1757.

The final published version is available online at: https://doi.org/10.1021/acscatal.0c04871

Momentum for Catalysis: How Surface Reactions Shape the RuO_2 Flat Surface State

Vedran Jovic,[1-3] Armando Consiglio,[4] Kevin E. Smith,[5] Chris Jozwiak,[1] Aaron Bostwick,[1] Eli Rotenberg,[1] Domenico Di Sante,[4] and Simon Moser[1,6,*]

1) *Advanced Light Source, E. O. Lawrence Berkeley National Laboratory, Berkeley, California 94720, USA*
2) *Institute of Geological and Nuclear Science, Wellington, 5012, New Zealand*
3) *School of Chemical Sciences, The University of Auckland, Auckland 1010, New Zealand.*
4) *Institut für Theoretische Physik und Astrophysik and Würzburg-Dresden Cluster of Excellence ct.qmat, Universität Würzburg, 97074 Würzburg, Germany*
5) *Department of Physics, Boston University, Boston, Massachusetts 02215, USA*
6) *Physikalisches Institut and Würzburg-Dresden Cluster of Excellence ct.qmat, Universität Würzburg, Würzburg 97074, Germany*

* *simon.moser@physik.uni-wuerzburg.de*

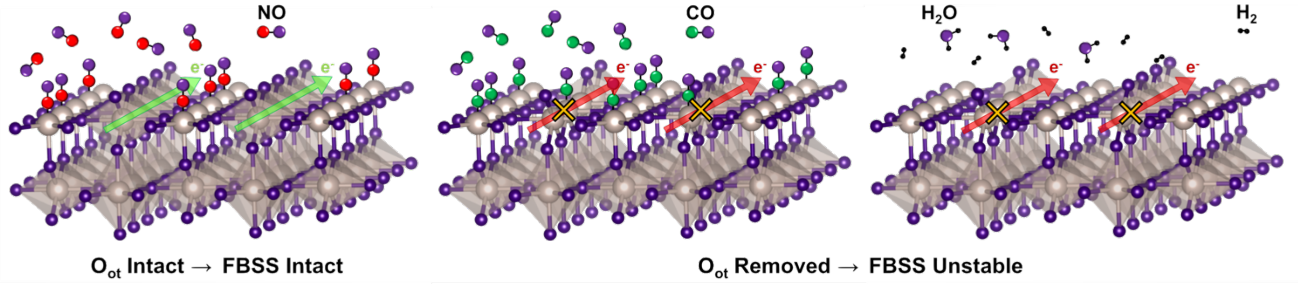

The active (110) surface of the benchmark oxygen evolution catalyst RuO_2 spans a flat-band surface state (FBSS) between the surface projections of its Dirac nodal lines (DNL) that define the electronic properties of this functional semimetal. Monitoring well known surface adsorption processes of H_2, O_2, NO and CO by *in-operando* angle resolved photoemission spectroscopy, we selectively modify the oxidation state of individual Ru surface sites and

identify the electronic nature of the FBSS: Stabilized by bridging oxygen O_{br} p_z, the FBSS disperses along <001> oriented chains of bridging Ru_{br} $4d_{z2}$ orbitals, collapses upon O_{br} removal, yet, remains surprisingly unaffected by the oxidation state of the undercoordinated 1f-cus-Ru species. This directly reflects in the ability of RuO_2 (110) to oxidize CO and H_2 along with its inability to oxidize NO, demonstrating the FBSS's active role in catalytic charge transfer processes at the oxygen bridge sites. Our synergetic approach provides momentum resolved insights to the interplay of a catalyst's delocalized electronic structure and the localized orbitals of its surface reactants – a route towards a microscopic understanding of heterogeneous catalysis.

Keywords. *– Ruthenium dioxide (RuO_2), angle resolved photoemission spectroscopy (ARPES), density functional theory (DFT), flat band surface state (FBSS), Dirac nodal lines (DNL), H_2 oxidation, CO oxidation, NO adsorption*

Introduction. **–** The (110) surface of ruthenium dioxide (RuO_2) serves as a useful study ground for a variety of catalytic oxidation and dehydrogenation reactions, summarized in two exemplar reviews by Over[1] and Weaver.[2] RuO_2 (110) is easily reduced in UHV and has been investigated as a prototypical oxidation catalyst for carbon monoxide (CO)[3] and nitrogen oxides (NO_x).[4,5] RuO_2 degrades alcohols,[6] and dehydrogenates ammonia (NH_3),[7] valuable properties to remediate wastewater.[8,9] The exceptional activity of RuO_2 (110) in the anodic evolution of chlorine is industrially exploited in the Deacon process, an energy neutral recycling method of Cl_2 from hydrochloric acid (HCl),[10–14] capable of replacing energy intense conventional recycling methods based on electrolysis.[1,15] With low overpotentials and – if alloyed with iridium[16] – high resilience in the anodic evolution of oxygen, RuO_2 has become the "gold standard co-catalyst" of electrolytic[17] and photocatalytic[18] water splitting, as well as of the electrochemical reduction of carbon dioxide (CO_2).[19]

Recently, the fundamental electronic and magnetic structure of RuO_2 has also gained attention due to the appearance of unusual and previously inaccessible physical phenomena such as colinear antiferromagnetism,[20–22] the crystal Hall effect[23,24] and Dirac Nodal lines (DNLs).[25–27] The latter underpin the semi-metallicity of this functional oxide and serve as anchors for a quasi-one-dimensional flat-band surface state (FBSS) at the (110) surface of RuO_2, which exhibits exaggerated – van Hove singularity like – density of states (DOS) right at the Fermi level (see Fig. 1a). The potential of this FBSS to act as a correlated reservoir of charge and spin[22,28] made us speculate about its role in surface catalytic charge transfer reactions,[27] however, a systematic experimental and theoretical study of its orbital origin and its interaction with surface reactants has remained elusive to date.

Here, we exploit four well characterized redox reactions to site selectively control the oxidation state of individual RuO_2 (110) surface atoms,[1,2] while we monitor the response of the valence electronic band structure *in-operando* by state-of-the-art angle resolved photoemission (ARPES): Hydrogen (H_2) and carbon monoxide (CO) act as reducing agents for surface Ru bridge sites (Ru_{br}) and destabilize the FBSS. Oxygen (O_2) and nitric oxide (NO) on the other hand adsorb on undercoordinated 1f-cus-Ru sites and leave the Ru_{br} sites and the FBSS unaffected. This demonstrates the FBSS to propagate along <001> oriented chains formed by bridging RuO_6 octahedra, where it actively participates in surface catalytic processes.

***Stoichiometric RuO_2 (110).* –** Bulk rutile RuO_2 is comprised of 6-fold coordinated Ru^{4+} cations and 3-fold coordinated O^{2-} anions. *In vacuo* cleaving of slightly *n*-type, 7% Ir doped, bulk RuO_2 single crystals with a ceramic top pin produces small (~50 μm), clean facets of a mostly stoichiometric (110) surface.[26,27] The *stoichiometric (110) surface* is depicted in Figure 1 (b1), exposing rows of fully (3-fold) coordinated oxygen (O_{3f}) and 2-fold coordinated bridging oxygen (O_{br}) species, as well as the 5-fold coordinated, i.e., 1-fold "coordinatively unsaturated" and partially reduced 1f-cus-Ru sites.

We have studied the electronic structure of this surface by micro-focused angle resolved photoemission spectroscopy (ARPES) with 69 eV photons and discussed the results in detail in Refs. 26 and 27. As summarized in the ARPES data of Figure 1(a), the FBSS disperses along the <001> direction but remains mostly localized, i.e., a flat band, along the perpendicular <110> direction. Density functional theory (DFT) calculations (see details in the method section) on a stoichiometric RuO_2 (110) surface slab (panel (b2) in Fig. 1 and Supporting Figs. 2-4) identify the predominant in-plane surface Ru_{br} d_{z2} and O_{br} p_z orbital character of the FBSS (inset), generating feature A in the surface DOS of panel (e) (see also Supporting Fig. 1).

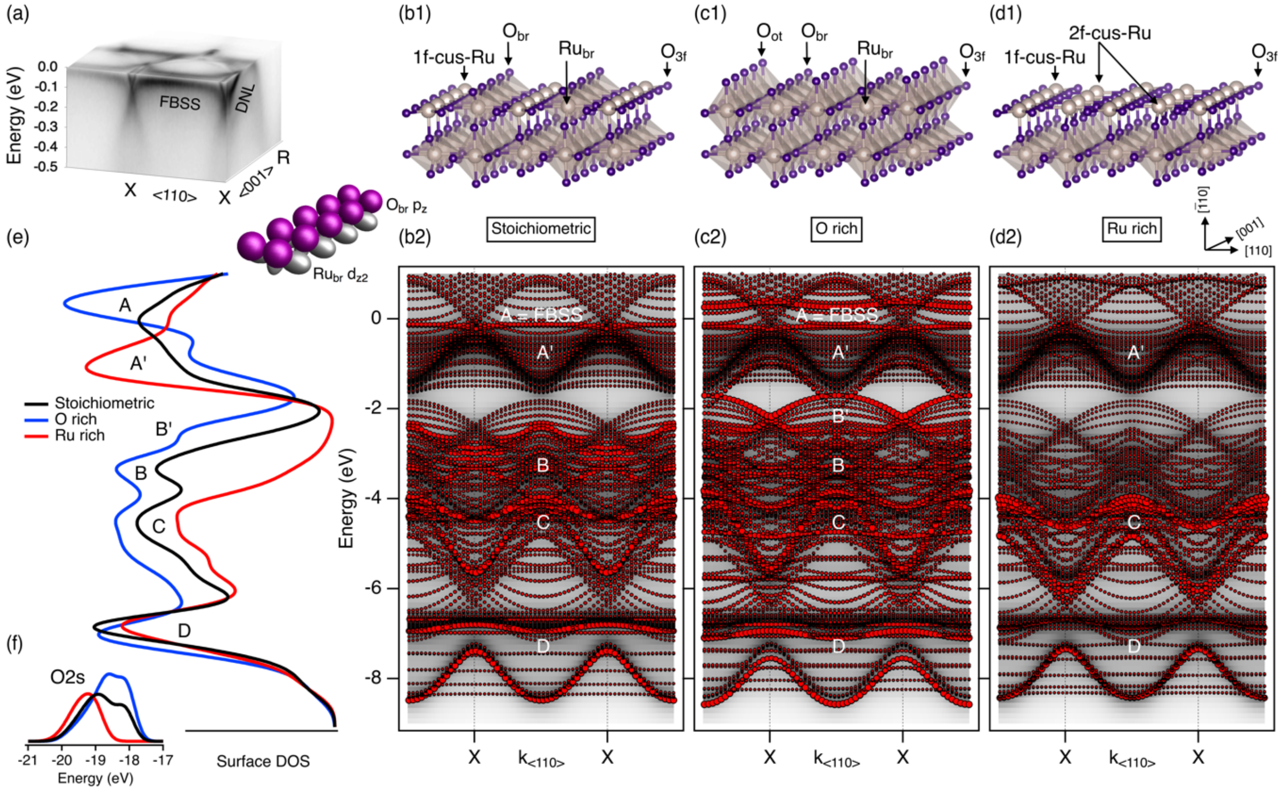

Figure 1: The FBSS on RuO_2 (110). (a) ARPES Fermi surface and maps along the XX and XR direction measured with 69 eV photons,[26,27] marking the DNLs and the FBSS that is spanned in between. (b-d) Crystal structure (1) and electronic DFT band structure (2) of the stoichiometric (b), the oxygen rich (c), and the ruthenium rich RuO_2 (110) surface (d). The marker size indicates the surface oxygen character, i.e., the

projection of the electronic bands onto the topmost O atomic orbitals to which ARPES at 69 eV (panel a) is most sensitive. The gray background is the surface projection of the bulk band structure. (e) Valence and (f) O 2s surface DOS of the stoichiometric (black), the oxygen rich (blue), and the ruthenium rich RuO_2 (110) surface (red) calculated by DFT. Feature "A" labels DOS of preliminary Ru $4d_{z2}$ character that forms the FBSS, feature "A' " the DOS composed of undersaturated Ru 4d states. Features "B", "B' " and "C" are of predominantly O 2p character and feature "D" of mixed orbital character (see supporting information).

Non-stoichiometric RuO_2 (110). – The under-coordinated 1f-cus-Ru sites have both electron donating and electron accepting character, and thus serve as active catalytic centers to bind a variety of surface reactants.[1,2] In particular, the 1f-cus-Ru site can bind 2-fold under-coordinated O_{ot} species via dissociative adsorption of molecular oxygen (O_2), resulting in an *oxygen rich surface* (Figure 1(c1)) that is expected to intensify the FBSS as well as the O_{3f} derived feature B' in the electronic band structure (Figure 1(c2) and (e)). Both O_{ot} as well as O_{br} act as proton acceptors that can be easily hydroxylated and – via subsequent diffusion, water formation and desorption[29,30] – removed by molecular hydrogen (H_2). This results in a *ruthenium rich surface* (Figure 1(d1))*,* leaving Ru_{br} sites exposed and reduced to 4-fold coordinated 2f-cus-Ru centers. The FBSS feature A as well as band B' are now expected to disappear, while the O_{3f} states condense into the higher energy band manifold C (see electronic properties in Fig. 1(d2) and Fig. 1(e)).

Having laid out the theoretical foundation, we now exploit this well-studied redox-process[1,2] to study the relationship of surface stoichiometry and the FBSS experimentally. The evolution of the RuO_2 (110) surface electronic structure upon room temperature H_2 exposure is summarized in Figure 2. We start from a freshly cleaved RuO_2 (110) surface in $<10^{-10}$ mbar UHV, aligned by ARPES along the reciprocal XX direction (cf. Fig. 1(a)). This surface is now exposed to $\sim 1.3 \times 10^{-8}$ mbar of H_2 (red), subsequently admixed and replaced by about the same amount of O_2 (blue) before the sample is pumped back to UHV. The temporal evolution of the partial gas pressures, tracked by a rest gas analyzer (RGA), is shown in panel (a) of

Figure 2. Simultaneously, we monitor the evolution of the ARPES signature close to the Fermi level (b1)–(b7), as well as the angle integrated photoemission signal up to 25 eV binding energy (c1) and (c2), *in operando* with 69 eV photons.

Panel (b1) shows the evolution of a momentum distribution curve (MDC) at the Fermi energy, i.e., the Fermi surface cut along XX; panel (b2) the evolution of an energy distribution curve (EDC) at a momentum right in between the two X points (vertical dashed line in b1). Panels (b3)–(b7) are representative ARPES images (cf. Fig. 1(a)) along the *colored horizontal lines* in panels (a), (b1) and (b2): specifically, for the pristine- (b3, black), the H_2- (b4, red), the H_2+O_2- (b5, purple) and the O_2 exposed surface (b6, blue), as well as the final measurement in UHV (b7, gray). While the bulk derived DNLs at X are robust upon all gas exposure (b1), the FBSS collapses upon exposure to H_2 (b1, b2, b4), but recovers upon admixture of O_2 (b1, b2, b5). As expected from theory (Fig. 1(c2)), dissociation of O_2 to O_{ot} shifts valence band spectral weight B' centered at -3.5 eV (black dotted guide to the eye in (b3)) upwards by ~ 0.5 eV (blue arrow in (b5)). This oxidation step is somewhat reverted in the final UHV step (b5), a sign of photo-stimulated O_{ot} desorption due to the collimated x-ray beam.[31]

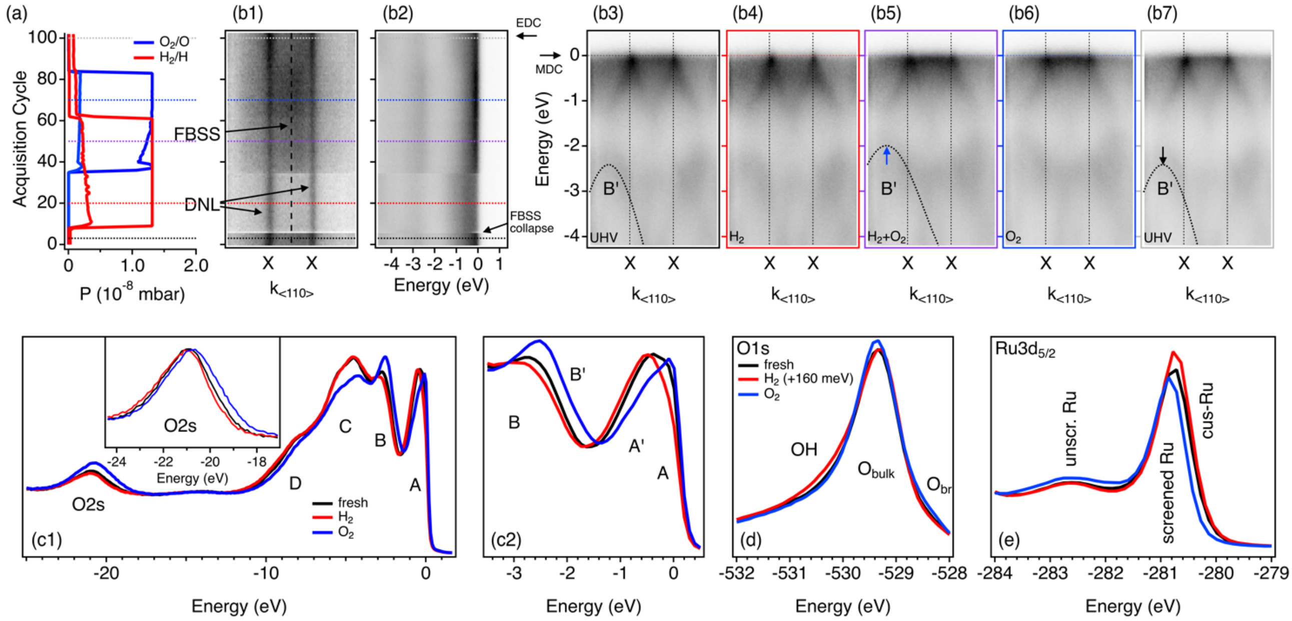

Figure 2: Dissociation of H_2 and O_2 on RuO_2 (110). (a) Evolution of H_2 and O_2 partial pressures in the ARPES chamber. One acquisition cycle corresponds to ~45 seconds. (b1) Evolution of the Fermi surface MDC along XX measured with 69 eV photons. (b2) Evolution of the EDC taken along the dashed vertical line in (b1). Panels (b3-b7) show representative ARPES images in UHV (b3, b7), in H_2 (b4), in H_2 + O_2 (b5) and O_2 (b6), taken along the color-coded horizontal lines in panels (a, b1, b2). Panels (c1, c2) show representative angle integrated spectra in UHV (black), in H_2 (red), and in O_2 (blue), taken at the color-coded horizontal lines in panels (a, b1, b2). (d) O1s and (e) Ru3$d_{5/2}$ core levels measured with 650 eV photons. The red spectrum in (d) was shifted by +160 meV.

Panel (c1) shows representative angle integrated photoemission spectra, revealing changes of the four major contributions to the valence surface DOS that were predicted by theory in Fig. 1(e): at ~-9 eV (feature D); at ~-5 eV (feature C); at ~-2.2 eV (feature B); and close to the Fermi level, feature A, the latter two which split into (A,A’) and (B,B’) upon closer inspection (c2). While H_2 (red) leaves peak C unaffected with respect to the freshly cleaved surface (black), it significantly suppresses upon O_2 exposure (blue). Feature B – built mostly from spectral weight of the dispersive band B in panels (b3)–(b7) – is slightly suppressed by H_2, but greatly enhanced and shifted by ~0.1 eV upon O_2 exposure (c2), forming the high energy shoulder B’ predicted by DFT. Further, H_2 considerably depletes Fermi level spectral weight of feature A (c2), which recovers and significantly sharpens at the expense of A’ (i.e., undersaturated Ru 4d states) upon exposure to O_2, as reflected in (b3)–(b7). The surface sensitive O 2s peak at ~-20.6 eV (the mean free path of photoelectrons at 50 eV kinetic energy is ~ 5 Å) is slightly reduced by H_2 but is greatly enhanced and broadened towards low energy by O_2, indicating additional surface oxygen as predicted in Fig. 1(f).

To check the surface stoichiometry more accurately, we repeat this gas dosing experiment on a fresh surface, this time monitoring the O 1s (panel (d)) and Ru 3d core levels (panel (e)) with 650 eV photons. With respect to the pristine surface (black), H_2 (red) shifts the O 1s peak in panel (d) towards 160 meV higher energy and produces a high energy shoulder, indicative of OH-group formation. O_2 removes these OH-groups, and – similar to the O 2s peak – enhances the O 1s main peak (the mean free path at this kinetic energy is less surface sensitive as for O 2s: ~ 10 Å), while simultaneously producing a small low energy shoulder indicative of additional surface oxygen.[29,30] In the Ru $3d_{5/2}$ manifold of panel (e), H_2 considerably enhances the screened main peak and its low energy shoulder, but leaves the unscreened satellite mostly unaffected, a sign of increased surface metallicity.[32] O_2 on the other hand re-oxidizes the surface, removes the 1f-cus-Ru-derived low energy shoulder and lowers the main peak in favor of the unscreened satellite.[33,34]

These observations are fully aligned with the expected redox scenario[1,2,35] and our theory: The initial hydroxylation of surface oxygen (OH-shoulder in O 1s peak) triggers the formation and desorption of water, removing surface oxygen species and producing a ruthenium rich surface (1-cus-Ru shoulder in Ru $3d_{5/2}$). The FBSS collapses and only recovers upon subsequent exposure to O_2, well known to bidentately adsorb and dissociate on neighboring 1f-cus Ru sites with reported O_{ot} coverages >86%, while efficiently replenishing O_{br} vacancies.[30] The Ru $3d_{5/2}$ low energy shoulder hence diminishes[33,34] in panel (e) in favor of the low energy O 1s and O 2s edges in panels (c1) and (d).[29,30] The consequent decrease in surface metallicity reduces screening and enhances the unscreened Ru $3d_{5/2}$ satellite.

The consistency of our experimental observations and theory allows us to conclude on the FBSS to stabilize on the stoichiometric and oxygen rich surfaces, but to collapse upon removal of O_{br} species. We can now further identify the O_{3f} derived surface DOS feature C as a useful indicator for the presence of coordinatively unsaturated cus-Ru sites, while B' foremost monitors the amount of on-top surface oxygen.

NO adsorption. – The adsorption of NO to the RuO_2 (110) surface is important for the understanding of catalytic oxidation of ammonia or NO_x exhaust emissions and is quite well understood:[2,35,36] Upon exposure to small amounts, NO molecules adsorb and bond strongly at 1f-cus-Ru species with the molecular axis oriented normally to the surface and nitrogen pointing towards ruthenium.[37–40] This bonding mechanism is commonly rationalized by purely local pictures within the Blyholder-[41] or more accurate three-orbital models.[36] In a nutshell, NO transfers charge from its 5σ to the Ru 4d states, an antibonding interaction that is counterbalanced by a bonding back-donation to the NO 2π* orbital. The dissociation of NO on two adjacent 1f-cus-Ru sites can produce adsorbed atomic nitrogen and oxygen species, which in principal – dependent on the reaction conditions – can react to adsorbed N_2, to N_2O as well as to NO_x and NO_2.[2,42]

We exploit this mechanism and monitor the response of the RuO_2 surface electronic structure to the adsorption of NO at room temperature in Fig. 3. In analogy to H_2 dosing, we start from a freshly cleaved, i.e., an essentially stoichiometric RuO_2 (110) surface in $<10^{-10}$ mbar UHV (black). This time, the surface is exposed to $\sim 1.3 \times 10^{-8}$ mbar of NO gas (red), successively admixed (purple) and replaced (blue) by about the same amount of O_2 before the chamber is pumped back to UHV. The partial pressure evolution measured by the RGA is shown in panel (a). As in the H_2 experiment, we monitor the ARPES signature close to the Fermi level (panels (b), (b1)–(b4)) as well as the integrated photoemission signal up to ~ 25 eV binding energy (panels (c), (c1) and (c2)) with 69 eV photons.

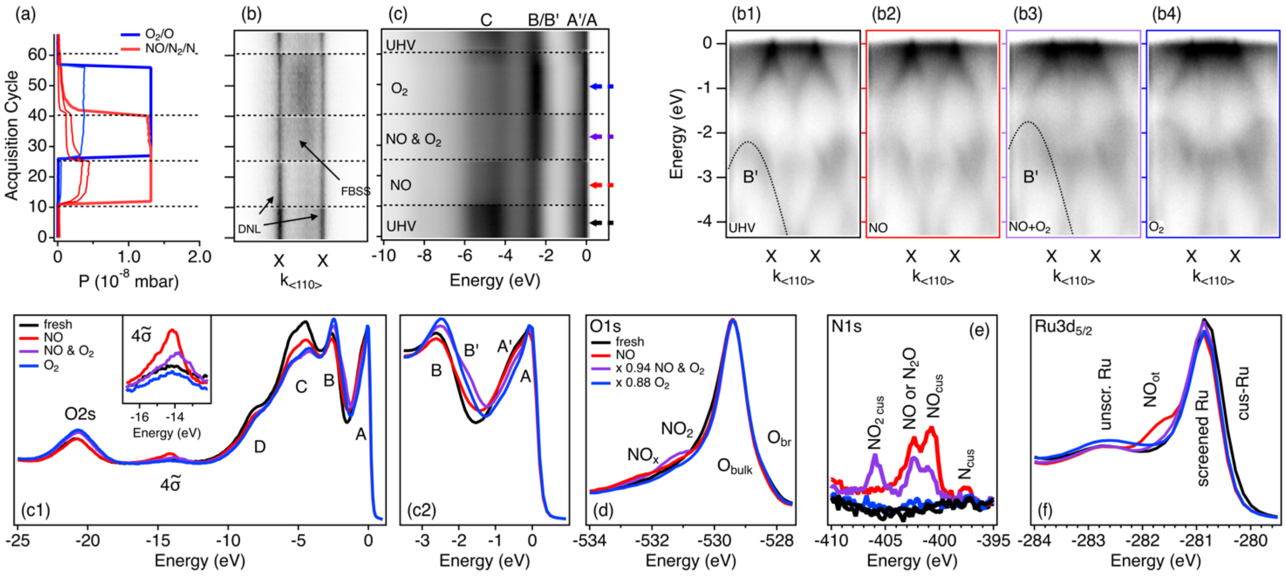

Figure 3: Adsorption of NO on RuO$_2$ (110). (a) Evolution of NO and O$_2$ partial pressures in the ARPES chamber. One acquisition cycle corresponds to ~49 seconds. (b) Evolution of a Fermi surface cut along XX measured with 69 eV photons. Panels (b1-b4) show representative ARPES images in UHV (b1), in NO (b2), in NO + O$_2$ (b3) and O$_2$ (b4), taken along the color-coded arrows panel (c). (c) Evolution of the angle integrated photoemission signal measured with 69 eV photons. Panels (c1, c2) show representative spectra in UHV (black), in NO (red), in NO + O$_2$ (purple) and in O$_2$ (blue), taken along the color-coded arrows in panel (c). (d) O1s, (e) N1s and (e) Ru3d$_{5/2}$ core levels measured with 650 eV photons. The blue and purple spectra in (d) were scaled by indicated factors.

Panel (b) shows the evolution of the Fermi surface MDC along XX and panels (b1)–(b4) are representative ARPES cuts of the pristine- (b1), the NO- (b2) the NO+O$_2$-, (b3) as well as the merely O$_2$ exposed surface (b4). While the DNLs *and, this time, the FBSS* remain robust upon NO exposure, O$_2$ intensifies the FBSS and shifts feature B' upwards by ~500 meV. Four representative angle-integrated spectra in panels (c1) and (c2) reveal the response of the valence band to individual gases (colored arrows in (c)). In contrast to H$_2$, NO (red) significantly suppresses feature C with respect to the fresh surface (black), a trend that continues upon further exposure to O$_2$ (blue). Peak B is slightly reduced by NO, but greatly enhances and shifts by ~0.1 eV upon O$_2$ exposure (c2), forming a high energy shoulder B' that mimics the shift of feature B' in panel (b3). Feature A, composed mostly of the FBSS, remains robust upon NO exposure (red in panel (c2)), but sharpens considerably with admixture of oxygen (purple, blue in panel (c2)).

At ~ -14.2 eV, NO produces a feature attributed to $4\tilde{\sigma}$ states of NO molecules bound to 1f-cus-Ru sites.[37–39] This peak is suppressed and shifted by ~500 meV upon O_2 admixture (purple, blue, inset in panel c1), marking a change in the surface bond. The O 2s peak at ~-20.6 eV remains unaffected by NO but intensifies and forms a low energy tail upon surface oxidation.

To gain further insight on the origin of this behavior, we monitor the O 1s (d), the N 1s (e) as well as the Ru 3d (f) core levels on a fresh surface with 650 eV photons. Exemplary spectra are shown for the fresh (black) as well as the NO- (red), the NO & O_2- (purple) and the O_2 exposed surface, respectively. With respect to the pristine surface, NO slightly lowers the O_{br} tail of the O 1s peak, which recovers via surface re-oxidation by O_2.[29,30] NO further produces a broad high-energy shoulder, that accumulates at ~-531.36 eV upon simultaneous exposure to O_2 (purple) and flattens once NO is removed from the chamber (blue). This shoulder is indicative of various NO_x species, which we identify in more detail in the N1s spectra of panel (e):

Features at -402.4 eV and -400.6 eV appear upon NO exposure (red) and are identified with adsorbed NO (the former peak might also point to N_2O).[43,44] A smaller peak at ~-397.4 eV is consistent with atomic nitrogen stemming from NO dissociation on 1f-cus-Ru sites.[44] The admixture of O_2 removes this N-peak, lowers (in particular) the -400.6 eV NO peak and produces an additional (non-volatile) NO_2 peak at -406 eV,[43] all of which are completely suppressed by oxygen (blue).

The bonding sites of these NO_x species are identified in the Ru $3d_{5/2}$ spectra of panel (e). A pronounced shoulder on the low energy side of the Ru $3d_{5/2}$ indicates the large amount of under-coordinated 1f-cus-Ru sites on the pristine surface (black).[32–34] Upon exposure to NO (red), this shoulder is removed in favor of a pronounced structure on the high energy side along with a reduction of the main Ru $3d_{5/2}$ peak, confirming NO molecules to bind on top of 1f-cus-Ru (NO_{ot}). The admixture of O_2 (purple) leads to a competition of NO and O_2 for 1f-cus-Ru sites,[35] which reduces and – upon removal of NO – completely removes this shoulder. The final O_2 step (blue) almost fully oxidizes the surface, which lowers the main Ru $3d_{5/2}$ peak but enhances its unscreened satellite due to the decreased surface metallicity.[32]

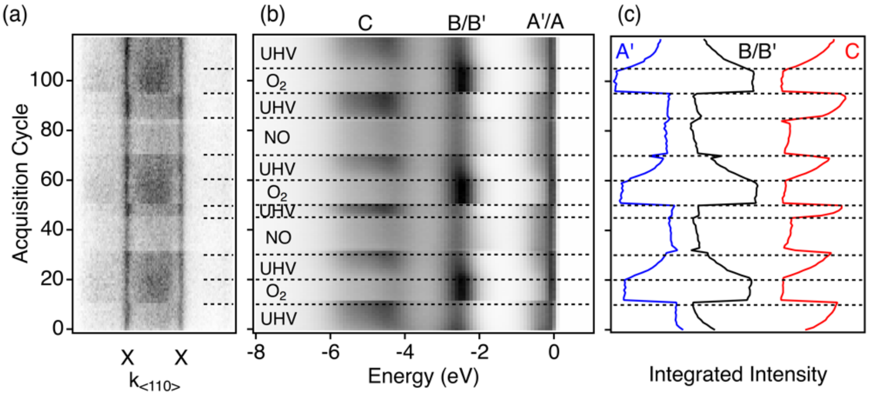

Figure 4: Cyclic adsorption of NO and O_2 on RuO_2 (110). (a) Evolution of a Fermi surface cut along XX measured with 69 eV photons. One acquisition cycle corresponds to ~49 seconds. (b) Evolution of the angle integrated photoemission signal measured with 69 eV photons. (c) Integrated spectral evolution of peaks C, B and the shoulder A'.

Interestingly, NO does not affect the FBSS, but only lowers valence peak C, a measure of the quantity of 1f-cus-Ru sites as we saw in the last section and as is confirmed in the behavior of the Ru $3d_{5/2}$ high energy shoulder. In contrast to hydrogen, NO *does not remove* O_{br}, strong experimental evidence for the FBSS to localize only along the <001> chains formed by O_{br} and Ru_{br}.

Rather than oxidizing NO, RuO_2 (110) was predicted to be an effective and reversible NO adsorber.[35] We thus test the reversibility of NO adsorption in Figure 4. The experiment is similar as above, but now built from several cycles of O_2 and NO exposure, interrupted by pumping cycles to ~10^{-10} mbar UHV. Panel (a) shows the evolution of the Fermi surface cut along the XX-line, panel (b) the evolution of the integrated valence band, and panel (c) the integrated signal of features A' (shoulder of A), B/B' and C. Additional valence band and core level data are consistent with our previous observations and shown in the supporting information.

We again start with a pristine surface with a pronounced shoulder A' to the FBSS A and a pronounced VB feature C. The first oxidation step instantly suppresses C and A', however, it enhances peak B (related to O_{br} species), indicative of an efficient oxidation of the 1f-cus-Ru surface sites. Assisted by the x-ray beam[31] and thermal energy,[30] the follow up UHV cycle reverts this process indicating beam assisted O_{ot} desorption.

Upon exposure to NO, peak C instantly decreases, while peak B and shoulder A' hardly change, as NO occupies only 1f-cus-Ru sites. A subsequent UHV cycle desorbs NO, before a new O_2 cycle re-oxidizes the 1f-cus-Ru sites. This proves the RuO_2 (110) surface to be a reversible NO adsorber under UHV conditions.[35]

CO adsorption and oxidation. – Another important model reaction catalyzed on the RuO_2 (110) surface is the oxidation of carbon monoxide.[1,2,35] CO has one electron less than NO but likewise strongly adsorbs with the C side down to 1f-cus-Ru through a donor-acceptor Blyholder mechanism.[41] Unlike NO, adsorbed CO – at sufficiently high temperatures – can react with both O_{ot} and O_{br} to volatile CO_2 species, which exposes 2f-cus-Ru sites that can bind further bridging CO.[1,2] We use this mechanism to reduce RuO_2 (110) and summarize its impact on the surface electronic structure in Figure 5.

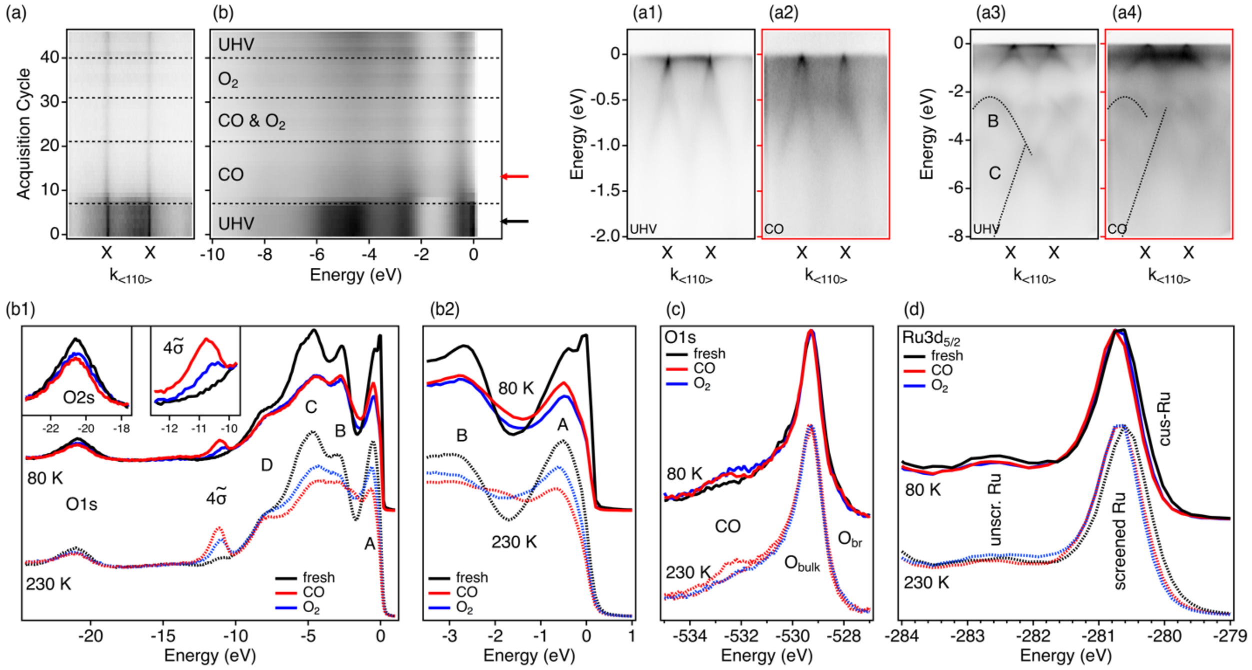

Figure 5: Adsorption of CO on RuO$_2$(110). (a) Evolution of a Fermi surface cut along XX measured with 69 eV photons. One acquisition cycle corresponds to ~56 seconds. Panels (a1-a4) show representative ARPES zoom- (a1, a2) and overview images (a3, a4) for UHV (a1, a3) and CO (a2, a4) exposure (color-coded arrows in panel b). (b) Evolution of the angle integrated photoemission signal measured with 69 eV photons. Panels (b1, b2) show representative overview (b1) and zoom in (b2) spectra in UHV (black), in NO (red), in NO + O$_2$ (purple) and in O$_2$ (blue) (color-coded arrows panel b), normalized to secondary electron background. (c) O1s (normalized to peak height) and (d) Ru3d$_{5/2}$ core levels measured with 650 eV photons.

Starting from a freshly cleaved and aligned RuO$_2$ (110) surface in <10^{-10} mbar UHV, we monitor both ARPES (panels (a), (a1) - (a4)) and angle integrated spectra (panels (b), (b1), (b2)) while the surface is exposed to ~1.3 × 10^{-8} mbar of CO (red), subsequently admixed and replaced by an equivalent amount of O$_2$ (blue), before pumping back to UHV (black). We start with data acquired at ~80 K and compare it to results obtained at ~230 K (dotted lines in (b1), (b2), (c) and (d)): Upon dosage with CO, both the FBSS (panels (a), (a1)–(a4)) and the overall spectral weight instantly collapse (panel b), while the secondary electron background increases – a sign of CO induced surface disorder. In contrast to our experiments with H$_2$ and NO, however, the signal does not fully recover upon later exposure to O$_2$ – particularly not at 80 K.

Similar to NO, the angle integrated spectra in panel (b1) (here normalized to secondary background) develop a $4\tilde{\sigma}$ peak at ~-10.8 eV (red) indicative of CO molecules bound to 1f-cus-Ru sites.[37–39] This peak is – irrespective of temperature – suppressed and shifted by ~300 meV, *but not removed* by O_2 (blue). A significant suppression of the O 2s peak at ~-20.6 eV indicates surface oxygen removal by CO (red), again remarkably unaffected by O_2 (blue), and again seen at both 80 and 230 K. This substitution of surface oxygen sites with CO is mimicked by the suppression of the valence features C, B and A, which only recover slightly upon O_2 exposure at 230 K. Interestingly, CO exposure shifts the dispersing band feature C in panels (a3) and (a4), a similar effect as we observed for surface oxidation in the previous sections.

In the 80 K O 1s core level of a fresh surface (solid lines in panel (c)), CO adsorption is reflected by the formation of a high energy tail (red), which gains weight upon further exposure to O_2 (blue). At 230 K, CO oxidation to volatile species is thermally more activated as compared to 80 K,[2] resulting in a reduction of the O 1s CO tail. The removal of the cus-Ru $3d_{5/2}$ shoulder and the reduction of the screened $Ru3d_{5/2}$ satellite in panel (d) reflects the irreversible coordination of surface cus-Ru sites with CO molecules at 80 K, while slightly activated CO oxidation at 230 K allows for the surface to somewhat re-oxidize (blue).

Impact. – Our results for the drosophila system RuO_2 (110) underline two important aspects: First, the modification of an ordered catalyst's surface band structure through site selective surface reactions can be used to monitor catalytic processes *in operando* and with *momentum resolution*. Second, but more importantly, the delocalized surface electronic band structure of the catalyst, i.e., *momentum carrying Bloch states*, actively participate in the catalytic process.

Tapping into this resource sheds new light on traditional tenets of surface chemistry, such as the fully local Blyholder picture, and offers new tools to bridge the gap between fundamental solid-state physics, surface chemistry and heterogeneous catalysis. In particular, our approach will prove valuable with respect to catalysts based on transition metal oxides, whose electronically active *d*-electrons are often subject to inherent many body effects[20,22,45] that directly reflect in the one-electron removal spectral function measured by ARPES. The method further assists in quantum engineering approaches based on topological principles, promising a route towards more effective catalysts.[46]

Whether topology and/or correlation physics such as magnetism affect surface reactions on RuO_2,[22,28] or other systems, is difficult to be answered experimentally and has yet to be shown. We point out, however, that such efforts will crucially depend on powerful spectroscopy tools based on VUV and soft X-rays that are available only at the synchrotron. In view of the current global upgrade to 4th generation diffraction limited storage rings of unprecedented brilliance along with novel end-stations, routine angle resolved experiments at near ambient conditions might become state-of-the-art in the long run. Endowed with additional time and spin resolution, such experiments could even give an *in operando* view on catalytic spin transfer and elucidate the role of surface magnetism in heterogeneous catalysis.[47]

Methods:

DFT-calculations. – Surface band structure calculations of the RuO_2 (110) surface were performed with the Vienna ab initio Simulation Package (VASP)[48,49] in the framework of Density Functional Theory, using the projector augmented wave method (PAW). Exchange and correlation effects were handled using the generalized gradient approximation (GGA) by

Perdew, Burke, and Ernzerhof (PBE).[50] While the effect of spin-polarization on the surface properties of RuO_2 is known from Ref. 28., we found satisfactory agreement with our ARPES results already at the non-spin-polarized level. Calculations have been performed using a plane wave cut-off of 600 eV on a $4 \times 4 \times 1$ k-point mesh, and SOC was included self-consistently. The slab consisted of 10 octahedral RuO_2 layers which account for a thickness of 32 Å. More than 10 Å of vacuum were included to screen the interaction between the repeated images in the periodic boundary conditions setting. The dimensions of the unit cell was $3.105 \ \times 6.359 \times 45.000\ \text{Å}^3$ and contained 60 atoms (20 Ru + 40 O) in the stoichiometric case, 62 atoms (20 Ru + 42 O) in the oxygen rich case and 58 atoms (20 Ru + 38 O) in the ruthenium rich case. In every instance, the surface of the supercell has been relaxed such that the total force acting on each atom is smaller than 0.01 eV/Å. The width of the smearing is 0.2 eV and the Methfessel-Paxton method of order 1 has been used. Finally, DOS calculations have been performed using a $16 \times 16 \times 1$ *k*-point mesh and the tetrahedron method (with Blöchl corrections).

µARPES experiments. – were performed at the Microscopic and Electronic Structure Observatory (MAESTRO) of the Advanced Light Source (ALS) in Berkeley, USA. RuO_2 single crystals were grown by chemical vapor transport and are from the same batch as samples that we used in Refs. 26 and 27. Crystals were cleaved in ultra-high vacuum ($< 5 \times 10^{11}$ mbar), exposing small (~50 µm) clean (110) surface domains, as confirmed by Laue diffraction. Details on extensive physico-chemical characterisation of the RuO_2 single crystals is provided in the supporting information of Ref. 26 and in Ref. 27.

Data was collected with p-polarized light, employing a hemispherical Scienta R4000 electron analyzer. The beam spot size was ~20 µm in the photon energy range below 200 eV. The analyzer slit was oriented along the [110] crystal axis, with the [110] surface vector pointing towards the analyzer. The total energy and momentum resolution of the experimental setup was better than 20 meV and 0.01 Å^{-1}, respectively. In operando dosing of high purity gases (99.999%) was performed through a leak valve up to a pressure of ~1.3 × 10^{-8} mbar. The gas lines were purged prior to experiment. Gases in the chamber were monitored by a residual gas analyzer (RGA).

Associated Content

Supporting Information. – The Supporting Information is available free of charge on the ACS Publications website at DOI: xxx.

- Additional DFT slab calculations.
- Additional photoelectron spectroscopy data on NO cycling.

Author Information

Corresponding Author. – E-mail: simon.moser@physik.uni-wuerzburg.de.

ORCID. – Simon Moser: 0000-0003-0042-2214

Notes. – The authors declare no competing financial interest.

Acknowledgements

We thank Herbert Over and Hicham Idriss for valuable discussion and feedback on our work. S.M. acknowledges support by the Swiss National Science Foundation under Grant No. P300P2-171221. The Boston University program is supported by the Department of Energy under Grant No. DEFG02-98ER45680. This research further used resources of the Advanced Light Source, which is a DOE Office of Science User Facility under Contract No. DE-AC02-05CH11231. The DFT work was supported by the Deutsche Forschungsgemeinschaft (DFG, German Research Foundation)—Project-ID No. 258499086—SFB 1170 and through the

Würzburg-Dresden Cluster of Excellence on Complexity and Topology in Quantum Matter—ct.qmat Project-ID No. 390858490— EXC 2147. The authors acknowledge the Gauss Centre for Supercomputing e.V. for funding this project by providing computing time on the GCS Supercomputer SuperMUC at Leibniz Supercomputing Centre.

References

(1) Over, H. Surface Chemistry of Ruthenium Dioxide in Heterogeneous Catalysis and Electrocatalysis: From Fundamental to Applied Research. *Chem. Rev.* **2012**, *112* (6), 3356–3426. https://doi.org/10.1021/cr200247n.

(2) Weaver, J. F. Surface Chemistry of Late Transition Metal Oxides. *Chem. Rev.* **2013**, *113* (6), 4164–4215. https://doi.org/10.1021/cr300323w.

(3) Wang, J.; Fan, C. Y.; Jacobi, K.; Ertl, G. The Kinetics of CO Oxidation on RuO 2 (110): Bridging the Pressure Gap. *J. Phys. Chem. B* **2002**, *106* (13), 3422–3427. https://doi.org/10.1021/jp014109k.

(4) Wang, H.; Schneider, W. F. Adsorption and Reactions of NOx on RuO2(110). *Catal. Today* **2011**, *165* (1), 49–55. https://doi.org/10.1016/j.cattod.2010.11.046.

(5) Li, L.; Qu, L.; Cheng, J.; Li, J.; Hao, Z. Oxidation of Nitric Oxide to Nitrogen Dioxide over Ru Catalysts. *Appl. Catal. B Environ.* **2009**, *88* (1–2), 224–231. https://doi.org/10.1016/j.apcatb.2008.09.032.

(6) Radjenovic, J.; Bagastyo, A.; Rozendal, R. A.; Mu, Y.; Keller, J.; Rabaey, K. Electrochemical Oxidation of Trace Organic Contaminants in Reverse Osmosis Concentrate Using RuO2/IrO2-Coated Titanium Anodes. *Water Res.* **2011**, *45* (4), 1579–1586. https://doi.org/10.1016/j.watres.2010.11.035.

(7) Cui, X.; Zhou, J.; Ye, Z.; Chen, H.; Li, L.; Ruan, M.; Shi, J. Selective Catalytic Oxidation of Ammonia to Nitrogen over Mesoporous CuO/RuO2 Synthesized by Co-Nanocasting-Replication Method. *J. Catal.* **2010**, *270* (2), 310–317. https://doi.org/10.1016/j.jcat.2010.01.005.

(8) Li, M.; Feng, C.; Hu, W.; Zhang, Z.; Sugiura, N. Electrochemical Degradation of Phenol Using Electrodes of Ti/RuO2–Pt and Ti/IrO2–Pt. *J. Hazard. Mater.* **2009**, *162* (1), 455–462. https://doi.org/10.1016/j.jhazmat.2008.05.063.

(9) Chiang, L.-C.; Chang, J.-E.; Wen, T.-C. Indirect Oxidation Effect in Electrochemical Oxidation Treatment of Landfill Leachate. *Water Res.* **1995**, *29* (2), 671–678. https://doi.org/10.1016/0043-1354(94)00146-X.

(10) Iwanaga, K.; Seki, K.; Hibi, T.; Issoh, K.; Suzuta, T.; Nakada, M.; Mori, Y.; Abe, T. *The Development of Improved Hydrogen Chloride Oxidation Process*; 2004.

(11) Crihan, D.; Knapp, M.; Zweidinger, S.; Lundgren, E.; Weststrate, C. J.; Andersen, J. N.; Seitsonen, A. P.; Over, H. Stable Deacon Process for HCl Oxidation over RuO2. *Angew. Chemie - Int. Ed.* **2008**, *47* (11), 2131–2134. https://doi.org/10.1002/anie.200705124.

(12) Zweidinger, S.; Crihan, D.; Knapp, M.; Hofmann, J. P.; Seitsonen, A. P.; Weststrate, C. J.; Lundgren, E.; Andersen, J. N.; Over, H. Reaction Mechanism of the Oxidation of HCl over RuO 2 (110). *J. Phys. Chem. C* **2008**, *112* (27), 9966–9969. https://doi.org/10.1021/jp803346q.

(13) Seki, K. Development of RuO2/Rutile-TiO2 Catalyst for Industrial HCl Oxidation Process. *Catal. Surv. from Asia* **2010**, *14* (3–4), 168–175. https://doi.org/10.1007/s10563-010-9091-7.

(14) Teschner, D.; Farra, R.; Yao, L.; Schlögl, R.; Soerijanto, H.; Schomäcker, R.; Schmidt, T.; Szentmiklósi, L.; Amrute, A. P.; Mondelli, C.; Pérez-Ramírez, J.; Novell-Leruth, G.; López, N. An Integrated Approach to Deacon Chemistry on RuO 2-Based Catalysts. *J. Catal.* **2012**, *285* (1), 273–284. https://doi.org/10.1016/j.jcat.2011.09.039.

(15) Trasatti, S. Electrocatalysis: Understanding the Success of DSA®. *Electrochim. Acta* **2000**, *45* (15–16), 2377–2385. https://doi.org/10.1016/S0013-4686(00)00338-8.

(16) Kötz, R.; Stucki, S. Stabilization of RuO2 by IrO2 for Anodic Oxygen Evolution in Acid Media. *Electrochim. Acta* **1986**, *31* (10), 1311–1316. https://doi.org/10.1016/0013-4686(86)80153-0.

(17) Lee, Y.; Suntivich, J.; May, K. J.; Perry, E. E.; Shao-Horn, Y. Synthesis and Activities of Rutile IrO 2 and RuO 2 Nanoparticles for Oxygen Evolution in Acid and Alkaline Solutions. *J. Phys. Chem. Lett.* **2012**, *3* (3), 399–404. https://doi.org/10.1021/jz2016507.

(18) Inoue, Y. Photocatalytic Water Splitting by RuO2-Loaded Metal Oxides and Nitrides with D0- and D10 -Related Electronic Configurations. *Energy Environ. Sci.* **2009**, *2* (4), 364. https://doi.org/10.1039/b816677n.

(19) Karamad, M.; Hansen, H. A.; Rossmeisl, J.; Nørskov, J. K. Mechanistic Pathway in the Electrochemical Reduction of CO 2 on RuO 2. *ACS Catal.* **2015**, *5* (7), 4075–4081. https://doi.org/10.1021/cs501542n.

(20) Berlijn, T.; Snijders, P. C.; Delaire, O.; Zhou, H.-D.; Maier, T. A.; Cao, H.-B.; Chi, S.-X.; Matsuda, M.; Wang, Y.; Koehler, M. R.; Kent, P. R. C.; Weitering, H. H. Itinerant Antiferromagnetism in RuO2. *Phys. Rev. Lett.* **2017**, *118* (7), 077201. https://doi.org/10.1103/PhysRevLett.118.077201.

(21) Zhu, Z. H.; Strempfer, J.; Rao, R. R.; Occhialini, C. A.; Pelliciari, J.; Choi, Y.; Kawaguchi, T.; You, H.; Mitchell, J. F.; Shao-Horn, Y.; Comin, R. Anomalous Antiferromagnetism in Metallic RuO2 Determined by Resonant X-Ray Scattering. *Phys. Rev. Lett.* **2019**, *122* (1), 017202. https://doi.org/10.1103/PhysRevLett.122.017202.

(22) Ahn, K.-H.; Hariki, A.; Lee, K.-W.; Kuneš, J. Antiferromagnetism in <math> <msub> <mi>RuO</Mi> <mn>2</Mn> </Msub> </Math> as <math> <mi>d</Mi> </Math> -Wave Pomeranchuk Instability. *Phys. Rev. B* **2019**, *99* (18), 184432. https://doi.org/10.1103/PhysRevB.99.184432.

(23) Šmejkal, L.; González-Hernández, R.; Jungwirth, T.; Sinova, J.; Gonz, R. Crystal Hall Effect in Collinear Antiferromagnets. **2019**, 1–10.

(24) Feng, Z.; Zhou, X.; Šmejkal, L.; Wu, L.; Zhu, Z.; Guo, H.; González-Hernández, R.; Wang, X.; Yan, H.; Qin, P.; Zhang, X.; Wu, H.; Chen, H.; Jiang, C.; Coey, M.; Sinova, J.; Jungwirth, T.; Liu, Z. Observation of the Crystal Hall Effect in a Collinear Antiferromagnet. **2020**, 1–24.

(25) Sun, Y.; Zhang, Y.; Liu, C.-X.; Felser, C.; Yan, B. Dirac Nodal Lines and Induced Spin Hall Effect in Metallic Rutile Oxides. *Phys. Rev. B* **2017**, *95* (23), 235104. https://doi.org/10.1103/PhysRevB.95.235104.

(26) Jovic, V.; Koch, R. J.; Panda, S. K.; Berger, H.; Bugnon, P.; Magrez, A.; Smith, K. E.; Biermann, S.; Jozwiak, C.; Bostwick, A.; Rotenberg, E.; Moser, S. Dirac Nodal Lines and Flat-Band Surface State in the Functional Oxide RuO2. *Phys. Rev. B* **2018**, *98* (24), 241101. https://doi.org/10.1103/PhysRevB.98.241101.

(27) Jovic, V.; Koch, R. J.; Panda, S. K.; Berger, H.; Bugnon, P.; Magrez, A.; Thomale, R.; Smith, K. E.; Biermann, S.; Jozwiak, C.; Bostwick, A.; Rotenberg, E.; Di Sante, D.;

Moser, S. The Dirac Nodal Line Network in Non-Symmorphic Rutile Semimetal RuO2. *arXiv Prepr. arXiv 1908.02621* **2019**.

(28) Torun, E.; Fang, C. M.; de Wijs, G. a.; de Groot, R. a. Role of Magnetism in Catalysis: RuO2 (110) Surface. *J. Phys. Chem. C* **2013**, *117* (12), 6353–6357. https://doi.org/10.1021/jp4020367.

(29) Knapp, M.; Crihan, D.; Seitsonen, A. P.; Resta, A.; Lundgren, E.; Andersen, J. N.; Schmid, M.; Varga, P.; Over, H. Unusual Process of Water Formation on RuO 2 (110) by Hydrogen Exposure at Room Temperature. *J. Phys. Chem. B* **2006**, *110* (29), 14007–14010. https://doi.org/10.1021/jp0626622.

(30) Knapp, M.; Crihan, D.; Seitsonen, A. P.; Lundgren, E.; Resta, A.; Andersen, J. N.; Over, H. Complex Interaction of Hydrogen with the RuO 2 (110) Surface. *J. Phys. Chem. C* **2007**, *111* (14), 5363–5373. https://doi.org/10.1021/jp0667339.

(31) Herd, B.; Abb, M.; Over, H. Photo-Induced Morphology Changes at the RuO2(110)/TiO2(110) Surface: A Scanning Tunneling Microscopy Study. *Top. Catal.* **2017**, *60* (6–7), 533–541. https://doi.org/10.1007/s11244-016-0711-y.

(32) Kim, H.-D.; Noh, H.-J.; Kim, K. H.; Oh, S.-J. Core-Level X-Ray Photoemission Satellites in Ruthenates: A New Mechanism Revealing The Mott Transition. *Phys. Rev. Lett.* **2004**, *93* (12), 126404. https://doi.org/10.1103/PhysRevLett.93.126404.

(33) Over, H.; Seitsonen, A. P.; Lundgren, E.; Wiklund, M.; Andersen, J. . Spectroscopic Characterization of Catalytically Active Surface Sites of a Metallic Oxide. *Chem. Phys. Lett.* **2001**, *342* (5–6), 467–472. https://doi.org/10.1016/S0009-2614(01)00627-3.

(34) Over, H.; Seitsonen, A. P.; Lundgren, E.; Smedh, M.; Andersen, J. N. On the Origin of

the Ru-3d5/2 Satellite Feature from RuO2(). *Surf. Sci.* **2002**, *504*, L196–L200. https://doi.org/10.1016/S0039-6028(01)01979-3.

(35) Wang, H.; Schneider, W. F. Comparative Chemistries of CO and NO Oxidation over RuO 2 (110): Insights from First-Principles Thermodynamics and Kinetics. *Mol. Simul.* **2012**, *38* (8–9), 615–630. https://doi.org/10.1080/08927022.2012.671521.

(36) Nilsson, A.; Pettersson, L. G. M. Chemical Bonding on Metal Surfaces. In *Model Systems in Catalysis*; Rioux, R., Ed.; Springer New York: New York, NY, 2010; pp 253–274. https://doi.org/10.1007/978-0-387-98049-2_12.

(37) Staufer, M.; Birkenheuer, U.; Belling, T.; Nörtemann, F.; Rösch, N.; Stichler, M.; Keller, C.; Wurth, W.; Menzel, D.; Pettersson, L. G. M.; Föhlisch, A.; Nilsson, A. Interpretation of X-Ray Emission Spectra: NO Adsorbed on Ru(001). *J. Chem. Phys.* **1999**, *111* (10), 4704–4713. https://doi.org/10.1063/1.479232.

(38) Stichler, M.; Keller, C.; Heske, C.; Staufer, M.; Birkenheuer, U.; Rösch, N.; Wurth, W.; Menzel, D. X-Ray Emission Spectroscopy of NO Adsorbates on Ru(001). *Surf. Sci.* **2000**, *448* (2–3), 164–178. https://doi.org/10.1016/S0039-6028(99)01232-7.

(39) Liu, Z.-P.; Hu, P.; Alavi, A. Mechanism for the High Reactivity of CO Oxidation on a Ruthenium–Oxide. *J. Chem. Phys.* **2001**, *114* (13), 5956–5957. https://doi.org/10.1063/1.1353584.

(40) Wang, Y.; Jacobi, K.; Ertl, G. Interaction of NO with the Stoichiometric RuO 2 (110) Surface. *J. Phys. Chem. B* **2003**, *107* (50), 13918–13924. https://doi.org/10.1021/jp0308108.

(41) Blyholder, G. Molecular Orbital View of Chemisorbed Carbon Monoxide. *J. Phys. Chem.* **1964**, *68* (10), 2772–2777. https://doi.org/10.1021/j100792a006.

(42) Jacobi, K.; Wang, Y. Interaction of NO with the O-Rich RuO2(110) Surface at 300K. *Surf. Sci.* **2009**, *603* (10–12), 1600–1604. https://doi.org/10.1016/j.susc.2008.09.047.

(43) Pashutski, A.; Folman, M. Low Temperature XPS Studies of NO and N2O Adsorption on Al(100). *Surf. Sci.* **1989**, *216* (3), 395–408. https://doi.org/10.1016/0039-6028(89)90383-X.

(44) Hornung, A.; Zemlyanov, D.; Muhler, M.; Ertl, G. The Catalytic Reduction of NO by H2 on Ru(0001): Observation of NHads Species. *Surf. Sci.* **2006**, *600* (2), 370–379. https://doi.org/10.1016/j.susc.2005.10.037.

(45) Zhu, Z. H.; Strempfer, J.; Rao, R. R.; Occhialini, C. A.; Pelliciari, J.; Choi, Y.; Kawaguchi, T.; You, H.; Mitchell, J. F.; Shao-Horn, Y.; Comin, R. Anomalous Antiferromagnetism in Metallic RuO2 Determined by Resonant X-Ray Scattering. *Phys. Rev. Lett.* **2019**, *122* (1). https://doi.org/10.1103/PhysRevLett.122.017202.

(46) Li, G.; Xu, Q.; Shi, W.; Fu, C.; Jiao, L.; Kamminga, M. E.; Yu, M.; Tüysüz, H.; Kumar, N.; Süß, V.; Saha, R.; Srivastava, A. K.; Wirth, S.; Auffermann, G.; Gooth, J.; Parkin, S.; Sun, Y.; Liu, E.; Felser, C. Surface States in Bulk Single Crystal of Topological Semimetal Co3Sn2S2 toward Water Oxidation. *Sci. Adv.* **2019**, *5* (8), 1–9. https://doi.org/10.1126/sciadv.aaw9867.

(47) Gracia, J.; Sharpe, R.; Munarriz, J. Principles Determining the Activity of Magnetic Oxides for Electron Transfer Reactions. *J. Catal.* **2018**, *361*, 331–338. https://doi.org/10.1016/j.jcat.2018.03.012.

(48) Kresse, G.; Joubert, D. From Ultrasoft Pseudopotentials to the Projector Augmented-Wave Method. *Phys. Rev. B* **1999**, *59* (3), 1758–1775. https://doi.org/10.1103/PhysRevB.59.1758.

(49) Kresse, G.; Furthmüller, J. Efficient Iterative Schemes for Ab Initio Total-Energy Calculations Using a Plane-Wave Basis Set. *Phys. Rev. B* **1996**, *54* (16), 11169–11186. https://doi.org/10.1103/PhysRevB.54.11169.

(50) Perdew, J. P.; Burke, K.; Ernzerhof, M. Generalized Gradient Approximation Made Simple. *Phys. Rev. Lett.* **1996**, *77* (18), 3865–3868. https://doi.org/10.1103/PhysRevLett.77.3865.